High Resolution Absolute Absorption Cross Sections of the $\tilde{B}^1A'-\tilde{X}^1A'$ Transition of the CH_2OO Biradical

Journal:	*Physical Chemistry Chemical Physics*
Manuscript ID	CP-ART-08-2015-004977.R2
Article Type:	Paper
Date Submitted by the Author:	07-Nov-2015
Complete List of Authors:	Foreman, Elizabeth; University of California, Irvine, Chemistry Kapnas, Kara; University of California, Irvine, Chemistry Jou, YiTien; University of California, Irvine, Chemistry Kalinowski, Jaroslaw; University of Helsinki, Chemistry Feng, David; University of California, Irvine, Mechanical and Aerospace Engineering Gerber, Benny; University of California, Irvine, Chemistry; University of Helsinki, Chemistry; Hebrew University, Chemistry Murray, Craig; University of California, Irvine, Chemistry

High Resolution Absolute Absorption Cross Sections of the $\tilde{B}^1A'$–$\tilde{X}^1A'$ Transition of the CH_2OO Biradical

Elizabeth S. Foreman,[1] Kara M. Kapnas,[1] YiTien Jou,[1] Jarosław Kalinowski,[2] David Feng,[3] R. Benny Gerber,[1,2,4,a] and Craig Murray[1,b]

1. *Department of Chemistry, University of California, Irvine, Irvine CA 92697, USA*
2. *Department of Chemistry, A.I. Virtasen aukio 1 (P.O. BOX 55) FI-00014, University of Helsinki, Finland*
3. *Department of Mechanical and Aerospace Engineering, University of California, Irvine, Irvine CA 92697, USA*
4. *Institute of Chemistry, Hebrew University, Jerusalem 91904, Israel*

---

[a] Email: benny@fh.huji.ac.il, Telephone: +972-2-651-3742
[b] Email: craig.murray@uci.edu; Telephone: +1-949-824-4218

Abstract

Carbonyl oxides, or Criegee Intermediates, are formed from the gas phase ozonolysis of alkenes and play a pivotal role in night-time and urban area atmospheric chemistry. Significant discrepancies exist among measurements of the strong $\tilde{B}^1A'$–$\tilde{X}^1A'$ electronic transition of the simplest Criegee intermediate, CH_2OO in the visible/near-UV. We report room temperature spectra of the $\tilde{B}^1A'$–$\tilde{X}^1A'$ electronic absorption band of CH_2OO acquired at higher resolution using both single-pass broadband absorption and cavity ring-down spectroscopy. The new absorption spectra confirm the vibrational structure on the red edge of the band that is absent from ionization depletion measurements. The absolute absorption cross sections over the 362-470 nm range are in good agreement with those reported by Ting *et al.*[1] Broadband absorption spectra recorded over the temperature range of 276–357 K were identical within their mutual uncertainties, confirming that the vibrational structure is not due to hot bands.

Introduction

Alkene ozonolysis plays a crucial role in the process of tropospheric oxidation and particle formation. Unsaturated hydrocarbons and ozone are consumed in the production of a stable carbonyl fragment and a highly internally excited carbonyl oxide, or Criegee intermediate.[2] The biradical/zwitterionic Criegee intermediate thermally decomposes to produce OH radicals and is also highly reactive with SO_2.[3–5] Criegee intermediates have long been thought to be key intermediates, but direct detection in the gas phase proved elusive until very recently. The first major breakthrough was the use of VUV radiation to selectively ionize the simplest Criegee intermediate, CH_2OO; but not its more stable isomers;[6,7] the second was production in the laboratory not by highly exothermic ozonolysis, but by the near thermoneutral reactions between iodoalkyl radicals and molecular oxygen. The rate constant for the latter reaction is up to six orders of magnitude larger than that for alkene ozonolysis,[8–10] which readily permits the production of large number densities of thermally stable Criegee intermediates. In the wake of these developments, there has been a surge of laboratory studies. The kinetics of the reaction of CH_2OO with trace atmospheric species have been followed using both direct and indirect detection. Spectroscopic detection of CH_2OO has now been achieved in the IR[11] and microwave regions,[12,13] with the latter approach conclusively demonstrating the formation of CH_2OO in ethene ozonolysis,[14] and in the visible/near UV.[1,8,15] The methyl-substituted CH_3CHOO biradical has also been detected in the near UV[16,17,18] and while it has been found to display conformer-specific reactivity to water vapor and SO_2,[18,19] its reactivity has been much less thoroughly explored than that of CH_2OO. Larger alkyl-substituted CIs appear to have very similar UV spectra.[20]

Our focus is the strong absorption band of CH_2OO in the visible and near-UV region that has been assigned to the $\tilde{B}^1A'$–$\tilde{X}^1A'$ electronic transition. Absorption in this region was first identified by Beames *et al.* using an action spectroscopy approach.[15] CH_2OO was produced by the reaction between photolytically-generated CH_2I and O_2 in a molecular beam and ionized using 118 nm VUV laser pulses. Depletion of the *m*/*z*=46 ion signal upon introduction of a second UV laser was monitored at discrete wavelengths over the range ~280–410 nm. An approximately Gaussian-shaped band was observed with maximum depletion at ~335 nm. The absolute absorption cross section of $\sim 5\times10^{-17}$ cm^2 at the peak was estimated based on the fluence of the UV depletion laser. Sheps later used time-resolved cavity-enhanced absorption spectroscopy (CEAS) to directly measure the absorption spectrum at a resolution of 2 nm, finding an absolute peak absorption cross section of $(3.6\pm0.9)\times10^{-17}$ cm^2 at ~360 nm. [8] The absorption band extended as far as ~440 nm and shows a regularly spaced vibrational progression on the red side that was attributed to long-lived vibrational levels of the $\tilde{B}^1A'$ state. Most recently, Ting et al. used a 750 mm long transient absorption spectrometer;[1] absolute absorption cross sections were determined using a depletion technique.[21] The peak cross section of $(1.23\pm0.18)\times10^{-17}$ cm^2 was found at 340 nm and the same vibronic structure was observed on the long-wavelength side. These measurements are shown in Figure 1. Qualitatively, the absorption measurements result in similar spectra, showing distinct vibronic band structure superimposed on an underlying continuum. Quantitatively, however, the peak absorption cross sections vary by at least a factor of three. The absence of the band structure seen in absorption from the depletion measurements indicates that the photodissociation quantum yield in this region is $\ll 1$. *Ab initio* calculations indicate that the $\tilde{B}$ state should support bound levels, with electronic predissociation facilitated by a conical intersection with repulsive surfaces at extended

OO distances.[22] These calculations indicate the intersection is located ~3000 cm^{-1} above the $\tilde{B}$ state minimum, suggesting that the predissociation rate may increase with vibrational excitation in the OO stretch mode. Hence, lower lying bound levels are expected to have a relatively slow predissociation rate and we might anticipate resolvable rotational structure in the absorption spectrum.

In this work, CH_2OO was prepared in a reaction flow cell by the reaction between photolytically generated CH_2I and O_2. Absolute absorption spectra of the structured region of the $\tilde{B}$–$\tilde{X}$ transition of CH_2OO at $\lambda > 360$ nm were measured with improved resolution using pulsed LEDs as broadband light sources, dispersed in a spectrograph. Additional absolute absorption spectra of selected low excitation energy vibronic bands of the $\tilde{B}$–$\tilde{X}$ transition, including the origin, were measured at high-resolution using pulsed laser cavity ring-down spectroscopy. Despite the higher resolution of our measurements we find no resolvable rotational structure in any of the bands, although the variation in the band contours is strongly suggestive of significant vibrational congestion in the spectrum.

Experimental Methods

Spectra were recorded by conventional single-pass absorption spectroscopy, using broadband pulsed LEDs as probe light source, and pulsed laser cavity ring-down spectroscopy. In both experimental arrangements, the photolysis laser beam was aligned to be collinear with the probe axis and steered through the reaction cell using dichroic mirrors that transmit $\lambda > 360$ nm.

Absorption spectra of CH_2OO were recorded by broadband transient absorption spectroscopy in a 50 cm long stainless steel flow cell. Measurements were made at 50 Torr total pressure, comprising 0.01% CH_2I_2, 7.3% O_2 and N_2 balance. All gas flows were regulated by calibrated mass flow controllers (Alicat) and the pressure monitored by a capacitance manometer (MKS). The photolysis laser was attenuated to provide approximately 9±1 mJ pulse^{-1} (32±4 mJ cm^{-2} fluence). The wavelength range 362–470 nm was covered by three probe LEDs with emission profiles nominally centered at 365, 405, and 455 nm. An LED driver (LightSpeed Technologies, Dragon HPLS-36DD18A) was used to generate short, broadband (duration < 8 μs, ~20 nm FWHM) light pulses that were initially coupled into a fiber optic and subsequently collimated using an achromatic doublet. After traversing the reaction cell, the transmitted probe light was focused onto the entrance slit of a spectrometer (resolution 0.12 nm) equipped with a low-noise, cooled CCD array camera (Andor SR303i with iDus 420). Spectra were collected at a 2 Hz repetition rate. Temperature was increased by wrapping flexible silicon rubber heating tape around the flow cell and insulating with aluminum foil. The flow cell was cooled by wrapping in an ice bath and insulating with rubber foam. Internal temperature of the reaction vessel was measured with a thermocouple with an estimated accuracy of ±2 K over the measured range.

High-resolution spectra of selected vibronic bands of CH_2OO were recorded using pulsed laser cavity ring-down spectroscopy (CRDS), also using collinear and counter-propagating photolysis-probe geometry. Spectra were collected at 70 Torr total pressure, 0.03% CH_2I_2, 5.4% O_2 and N_2 balance. The photolysis laser was unfocused and attenuated to 1.5±0.1 mJ pulse^{-1} (5.3±0.4 mJ cm^{-2} fluence) in order to avoid damage to the ring-down mirrors. Probe light in the wavelength range 417–435 nm was obtained from a Nd:YAG pumped dye laser (0.0014 nm bandwidth) operating with Stilbene 420 and Coumarin 440 dyes (Continuum ND6000 and Surelite III-10). The pulse energy was attenuated to < 20 μJ pulse^{-1} and coupled into the optical cavity, which comprised two highly reflective mirrors (nominal $R = 0.99995$ at a center wavelength of 440 nm) separated by 37.5 cm. The transmitted light was detected by a PMT and digitized by a 12-bit, 500 MHz digital oscilloscope (LeCroy HDO). Individual ring-down waveforms were fit to single exponential decays in real time. Absorption spectra were recorded by measuring the change in ring-down time relative to the "empty" ring-down time, $\tau_0(\lambda)$, as a function of dye laser wavelength:

$$\alpha(\lambda) = \frac{1}{\mathrm{c}}\left(\frac{1}{\tau(\lambda)} - \frac{1}{\tau_0(\lambda)}\right)$$

No evidence of ringing down was observed with only the photolysis beam present. The incident photolysis beam had no structural influence on $\tau_0(\lambda)$ in the empty reaction cell. Further details and diagnostics of the collinear and counter-propagating photolysis-probe CRDS apparatus are in the Supplementary Materials.

The empty cavity ring-down time was measured using a photolysis-probe delay of –20 ms, i.e. the photolysis laser was fired 20 ms *after* the probe laser, or 180 ms before the next cycle at the 5 Hz repetition rate. It was verified that the long-lived absorption due to IO is completely removed within 180 ms by monitoring IO absorption at the $A^2\Pi_{3/2}$–$X^2\Pi_{3/2}$ (4,0) bandhead as a function of delay (see Figure S4). Optimal delays for recording $\tau(\lambda)$ were determined in an analogous fashion and are discussed in detail alongside the results. We recorded ring-down times for all delays at each probe wavelength before stepping the dye laser, to achieving a "real time" background subtraction, which is advantageous during potentially lengthy spectral acquisitions.

Theoretical Methods

Even though CH_2OO in equilibrium is dominated by a single configuration wavefunction,[23] it has been shown that potential energy surface around minimum geometry exhibits major contributions of other electronic configurations and excited states proved to require multiconfigurational approach.[24] To satisfy this requirement in all calculations we used MRCI method as implemented in GAMESS.[25,26] An active space consisting of 12 electrons in 12 orbitals was used. Multi-level parallelism, introduced in our previous work, was used to improve the scalability of calculations.[27] We used Dunning's cc- pVTZ basis set, which is expected to give satisfactory results for this system.[28] To avoid numerical and convergence issues, state averaging was used with assumed equal weights for both $\tilde{B}^1A'$ and $\tilde{X}^1A'$ states.

The stability of vibrational spectrum calculations based on numerical Hessian was investigated by calculating numerical Hessians with different atom displacements ranging from 0.05 Å to 0.001 Å. Tested changes in displacements used did not affect the vibrational frequencies by more than 0.1 cm^{-1} suggesting that there is no risk of discontinuities in potential energy surface in an area relevant for the vibrational analysis. In addition, the convergence of the results in respect to the active space size was tested. Removing up to two occupied or virtual orbitals from the active space changed vibrational frequencies by less than 1 cm^{-1}.

Results and Discussion

CH_2OO was produced in a stainless steel reaction flow cell by the reaction between CH_2I radicals, generated by pulsed laser photolysis of CH_2I_2 at 355 nm, and molecular oxygen:

$$CH_2I_2 + h\nu \rightarrow CH_2I + I \quad (1)$$

$$CH_2I + O_2 \rightarrow CH_2OO + I \quad (2a)$$

$$CH_2I + O_2 \rightarrow HCHO + IO \quad (2b)$$

$$CH_2I + O_2 + M \rightarrow CH_2IOO + M \quad (2c)$$

$$CH_2OO + I \rightarrow HCHO + IO \qquad (3)$$

Linear absorption measurements are complicated slightly by the formation of IO radicals via reactions (2b) and (3).[1,18] Well-characterized bands associated with the $A^2\Pi_{3/2}$–$X^2\Pi_{3/2}$ transition of IO in the 360–470 nm range overlap the structured red wing of the CH_2OO absorption band. The background subtraction procedure exploits the very different kinetics of CH_2OO and IO formation and loss.

The structured region of the $\tilde{B}$–$\tilde{X}$ transition of CH_2OO recorded using conventional single-pass absorption spectroscopy is shown in Figure 2. The spectrum has been assembled from sequential measurements made using three different LEDs to span the 362–468 nm wavelength range, as shown in Figure 2(a). The spectral resolution of 0.12 nm is improved over previous absorption measurements which report an instrument resolution of 2 nm. A time delay of ~10 μs between the photolysis laser and LED probe pulse maximizes the contribution of CH_2OO to the spectrum, although features attributable to bands of the IO $A^2\Pi_{3/2}$–$X^2\Pi_{3/2}$ transition are clearly visible in Figure 2(b). CH_2OO and IO have very different kinetic behavior. At low pressures, CH_2OO + I are the major products and are formed directly via reaction (2a).[9,29] The range of reported rate constants for reaction (2) overall is $1.37–1.82\times10^{-12}$ cm^3 s^{-1}.[8,9,30,31] The CH_2OO population reaches a maximum at early times and is removed by rapid self-reaction and by reaction (3).[9,32,33] The latter reaction is largely, although not exclusively, responsible for the production of IO which increasingly contributes to the overall absorption spectrum at longer delay times. Measuring the rate of production of IO is complicated by contributions from both direct (2b) and indirect (3) reactions. Existing rate constants span the range $0.0026\text{-}3.5\times10^{-11}$ cm^3 s^{-1},[34–36] although a recent study[37] reports a phenomenological rate constant of $(1.5\pm0.1)\times10^{-13}$ cm^3 s^{-1} for the formation of IO due to all processes.

In order to remove the unwanted IO contribution, spectra were recorded independently by tuning the photolysis-probe delay to 100 μs, by which time CH_2OO has been completely consumed under the experimental conditions of this work. Comparison to previously recorded IO spectra[38,39] confirms the absence of any significant CH_2OO absorption at the longer delay. The early-time IO contribution can be readily removed from the overall absorption spectrum by scaling and subtracting the pure IO spectrum. The scaling factor can be determined either by matching the absorbance of features for which there is no overlap (e.g. the IO bands at $\lambda > 440$ nm) or from the ratio of IO absorbance at 10 μs and 100 μs from our previous study of the kinetics of the $CH_2I + O_2$ reaction performed under the same experimental conditions.[37] Both approaches yield consistent results. Absorption depletion caused by ~1% dissociation of the precursor molecule, CH_2I_2, was also considered, but would contribute less than <1.5% of the observed signal over the 362–468 nm range and has therefore been discounted.

The CH_2OO spectrum shown in Figure 2(c) is in excellent agreement with previous absorption spectroscopy measurements.[1,8] There are seven readily identifiable bands in this wavelength region; fitting to a sum of Lorentzian functions with an underlying Gaussian centered at 29627 cm^{-1}, yields an average separation of 608±39 cm^{-1}. Band centers and widths are listed in Table 1 alongside the peak assignments from Ting *et al.* for comparison. The FWHM varies over the range 140 to 417 cm^{-1}. While the spectrum can be reasonably decomposed using a sum of Lorentzian functions, closer inspection shows that the shapes of the band contours vary; an expanded view of the 376–406 nm region is shown in the inset in Figure 2(c). The widths of the bands are also significantly too broad to be attributed purely to homogeneous line broadening. While the progression is dominated by a component with frequency ~610 cm^{-1}, other modes must also show significant Franck-Condon activity and lead to significant vibrational congestion in the spectrum, as suggested originally by Sheps. The weak feature at ~431 nm appears to be the lowest frequency band; within the signal to noise there is no evidence of any additional features that can be attributed to CH_2OO at longer wavelengths and we tentatively assign this as the origin band. This region of the spectrum is rather noisy because of the overlap with the A–X(4,0) band of IO radicals and the subtraction procedure.[8]

Cavity ring-down spectroscopy provides both higher sensitivity and higher resolution (the dye laser linewidth is 0.08 cm^{-1} or ~0.0014 nm) than the single-pass broadband absorption technique. CRD spectra of the weak, lowest energy vibronic bands between 417–435 nm were recorded. These features, corresponding to excitation to levels lying deepest in the $\tilde{B}$ state well, were thought to be most likely to show resolvable rotational structure. Spectra were recorded at photolysis-probe delays of 8 and 140 μs. The heavily predissociated A–X(5,0) and (4,0) bands of IO contribute strongly to the absorption in this spectral region, as shown in Figure 3(a), even at early times. Spectra collected at the longer delay time of 140 μs contain contributions from IO exclusively. A scaling factor was determined from a transient absorption study under identical experimental conditions;[37] the ratio of IO absorption at the (3,0) band head at 8 μs and 140 μs indicates a factor of 0.15±0.1. After subtraction of the IO contribution, two broad and unstructured features are visible in Figure 3(b). The spectrum is again decomposed as a sum of two Lorentzian functions. We tentatively assign the band centered at 430.17 nm (23247 cm^{-1}) to the 0_0^0 origin band. The strong band at 419.53 nm (23836 cm^{-1}) is 589 cm^{-1} to the blue of the origin; it seems likely that the $\tilde{B}$ state vibrational mode responsible for this feature is the one that dominates the rest of the vibrational progression evident in the spectrum.

The absolute absorption cross section can be determined from an estimate of the peak CH_2OO number density present in cell according to the Beer-Lambert law. Several steps are required to estimate $n_{\mathrm{CH_2OO}}$ and these are described in detail in the Supplementary material. Briefly, we first measure the initial CH_2I_2 number density and estimate the photolysis yield of CH_2I from known laser fluence. The yield of CH_2OO via reaction 2(a) has been measured as a function of pressure by several groups. An additional correction is applied to account for the time-dependence of the CH_2OO number density. Resulting CH_2OO number densities for the BBTA and CRD measurements are $(1.4\pm0.39)\times10^{13}$ $\mathrm{cm^{-3}}$ and $(5.1\pm1.4)\times10^{12}$ $\mathrm{cm^{-3}}$, respectively, resulting in the absolute absorption cross sections shown in Figure 4. The uncertainty in the number density (~28%) estimate is easily the largest uncertainty in the absorption cross section determination. The small region of overlap between the broadband and CRDS experiments, 417–435 nm, shows excellent agreement, despite being measured under different experimental conditions, suggesting that the estimation method is reliable. Within their mutual uncertainties, the cross sections determined in this work are in excellent agreement with those of Ting *et al.* at all wavelengths within the 362–480 nm range, and in reasonable agreement with Beames *et al.* in the 374–383 nm range. Potential sources of error in the CH_2OO number density may arise from our calculated photolysis yield based on the photolysis laser fluence, or the branching of reaction (2a) measured by other groups. It is unlikely that any of these sources of error are significant enough to bring our measurements into agreement with the cavity-enhanced measurement of Sheps.

Ab initio calculations using the MRCI method have been used to optimize the geometries and predict harmonic vibrational frequencies for the $\tilde{X}^1A'$ and $\tilde{B}^1A'$ states of CH_2OO. The vertical excitation energy is calculated to be 3.66 eV, which, based on the reflection principle, would result in a maximum absorption cross section at 339 nm, in good agreement with experiment. The adiabatic excitation energy, after including harmonic zero-point energies (corresponding to the energy of the experimental 0_0^0 band) is 2.71 eV or 458 nm, which is slightly further to the red of the origin band identified in the CRD spectrum. There are however, significant geometry changes upon electronic excitation, in particular the terminal OO bond extends from 1.336 Å to 1.613 Å, while ∠(COO) decreases from 118.5° to 98.9°, and it remains possible that the origin band is not observed. The vibrational structure is therefore likely to be dominated by progressions in the OO stretch (ν_6) and COO bend (ν_7). Earlier TD-B3LYP/6-311++G** calculations by Lee *et al.* find similar geometry changes upon excitation; namely, an OO bond extension of from 1.353 Å to 1.623 Å and reduction of ∠(COO) from 119.6° to 90.5°.

Harmonic frequencies for both ground and excited states calculated using MRCI are collected in Table 2, alongside the earlier TD-DFT results of Lee et al.[40] Progressions based on ν_6 and ν_7 are most likely based on Franck-Condon arguments, although both the MRCI and TD-DFT calculations predict frequencies that bracket the observed separation of ~620 cm^{-1}. A warning flag regarding the MRCI calculations, however, is the anomalously large frequencies of ν_2 and ν_4, the symmetric CH stretch and a mixed CO stretch/CH_2 scissors mode. We have been able to find no obvious technical problems with the MRCI calculations and suggest that these may be the result of the proximity of the repulsive electronic states. While the TD-DFT calculations result in frequencies that are apparently more plausible, there is no *a priori* reason to expect this method to be more reliable. It is worth noting that in the excited state CO and CH stretching vibrations are highly coupled and large CH displacements present in CO/CH_2 mode for the excited state can explain extraordinarily high frequency for CO stretching type vibrations like ν_4.

The anticipated asymmetric top rotational contour for an individual band was simulated using PGOPHER[41]. Rotational constants A_0, B_0, and C_0 determined from microwave spectroscopy[12,13] were used for the $\tilde{X}^1A'$ state (77.75, 12.46, 10.72 GHz). Those for the $\tilde{B}^1A'$ state were derived from the optimized *ab initio* geometry (47.06, 12.30, 9.75 GHz,). Figure 5 shows simulations assuming a *a*-type and *b*-type transition dipole moments and excited state lifetimes of 0.1 ps, 1 ps and 10 ps, corresponding to homogeneous broadening of 53 cm^{-1}, 5.3 cm^{-1} and 0.53 cm^{-1}, respectively. Even with a relatively short excited state lifetime of 10 ps, we expect to be able to resolve the rotational structure in the CRD spectrum. Simulations assuming no lifetime broadening but performed at the lower resolution of the spectrometer (0.12 nm) appear very similar to the 1 ps lifetime-broadened spectra in Figure 5; the oscillations due to the K_a sub-bands would be visible in principle, albeit not within the signal to noise of the absorption spectrum shown in Figure 2. A short excited state lifetime is needed to completely wash out the rotational structure, while unphysically short lifetimes would be required to reproduce the ~150 cm^{-1} widths of the features observed in the experimental spectrum. Taken in conjunction with the variations in band contours, it seems likely that some degree of lifetime broadening is accompanied by significant spectral congestion arising from progressions in several vibrational modes.

There remains a discrepancy between the absorption spectra measured in this and other work[1,8] and the depletion measurements,[15] which are apparently blind to the vibrational structure at $\lambda >$ 360 nm. An important difference between the two types of measurements is that the latter were performed in a supersonic expansion and sample a cooled, but likely non-equilibrium, ensemble. Consequently, it has been suggested that the vibrational structure may be due to hot bands.[42] While this seems somewhat implausible given the energy range spanned by the vibrational structure is many times kT, we investigated the temperature dependence of the absorbance in the temperature range 276–357 K, using otherwise identical experimental conditions. The resulting spectra are shown in Figure 6. Aside from variations in the absolute absorbance, that can be attributed to changes in total CH_2OO number density, the spectra are identical within their mutual uncertainties. Assuming a thermal distribution, the population in the first excited levels of the four lowest frequency modes (see Table 1) increase ~67–182% over the limited temperature range explored. For example, the fractional population of the lowest lying vibrational level, ν_7, increases from 0.048 at 276 K to 0.079 at 357 K. The absence of any significant change in the wavelength-dependence of the absorption spectrum with temperature leads to the definitive conclusion that the observed vibrational progression cannot be attributed to hot bands, but rather to the excitation of bound levels of the $\tilde{B}$ state.

The implication is that the photolysis quantum yield in this wavelength region must be much less than unity. Sheps suggested that the relatively long-lived states responsible for the structure in the spectrum might subsequently relax by fluorescence or other non-radiative processes.[8] Ting *et al.* later argued against the existence of long-lived states on the basis that angular anisotropy of $O(^1D)$ photofragments indicated sub-ps excited state lifetimes.[43] However, this argument apparently neglects the fact that the longest photolysis wavelength used in the ion imaging study was 360 nm, which is the short wavelength onset of the structured region of the spectrum. To date, dissociation photoproducts have not been detected following excitation in the structured region at $\lambda > 360$ nm. The $\tilde{B}^1A'$ surface does however appear to support bound states in this excitation energy range. The electronic structure calculations at the MRCI-F12 level by Dawes *et al.*[22] predict a nonadiabatic well in the $\tilde{B}^1A'$ state of ~ 3000 cm^{-1}. The simulated absorption spectrum also shows evidence of a weak vibrational progression at low excitation energies, in broad agreement with the experimental observations, although somewhat less pronounced. In contrast, Samanta *et al.* predicted a broad and structureless absorption $\tilde{B}$–$\tilde{X}$ absorption spectrum.[44] It is likely that the DW-CASSCF is not sufficient to describe the regions of nonadiabatic curve crossings with local $^1A'$ states due to restrictions on active space and necessity for including dynamical electron correlation. Molecular dynamics simulations also suggest the existence of resonance states that have significant lifetimes and could be responsible for the vibrational structure. Although the number of calculated trajectories does not allow for proper statistics, the results indicate that less than 40% of excitation events sampled along the spectrum are expected to lead to decomposition of the species. The results of these calculations together with the analysis of multiconfigurational nature of the excited state will be described in a companion theoretically focused paper.

Here we attempt to rationalize the apparent discrepancy between the depletion and absorption measurements. Interpretation of the depletion measurement may be complicated by the dynamics in the $\tilde{B}^1A'$ state following excitation. A short radiative lifetime would return population to the ground state prior to VUV ionization and reduce the magnitude of the depletion signal. The radiative lifetime of the $\tilde{B}^1A'$ state can be estimated from the integrated absorption spectrum.[45] Using the measurement of Ting *et al.*, the radiative lifetime is estimated to be ~7 ns, significantly shorter than the 100 ns timescale of the depletion measurements. If non-radiative processes are uncompetitive, one may expect fluorescence to be observable after excitation in the structured region. A ns-scale lifetime would, however, means that the instrument functions (the spectrometer linear dispersion or dye laser bandwidth) would represent the limiting resolution in our measurements and rotational structure would be expected in the spectra. Some degree of lifetime broadening contributes to washing out the rotational structure, but it seems clear that a non-radiative process other than dissociation must be responsible. Furthermore, the non-radiative population transfer must transfer population to a state with a lifetime of order ~100 ns that also can be ionized with comparable efficiency to the ground state.

Intersystem crossing to nearby triplet states is likely to be too slow in the absence of second row or larger atoms. Internal conversion, on the other hand, could transfer population to either of the lower-lying singlet states ($\tilde{A}^1A''$ or $\tilde{X}^1A'$) via the exit channel conical intersections. Radiative transition between the $\tilde{A}^1A''$ state and the ground state is predicted to have much smaller oscillator strength and hence should have a significantly longer radiative lifetime.[40] A more speculative outcome is isomerization to a more stable isomer, such as dioxirane or formic acid. While the ionization potentials of these species are slightly larger (10.82 eV and 11.33 eV) than the 10.49 eV photon energy used in the depletion measurements, they would be formed with several eV of internal excitation and may be ionized readily.

Conclusion

The spectra of the $\tilde{B}$–$\tilde{X}$ transition of CH_2OO between 362–468 nm reported here are in agreement with those of Sheps and Ting *et al.,* which were recorded using similar absorption techniques but at lower resolution. Absolute absorption cross sections determined in this work agree well with those of Ting *et al*. The improved resolution of this study reveals no rotational structure within any of the vibrational bands, even those at the lowest excitation energies. The absence of the vibrational progression in the VUV depletion measurements of Beames *et al.,* coupled with the broad widths of the individual vibrational bands points to significant lifetime broadening. We suggest that the rapid excited state dynamics evidenced by broad bandwidths must be attributed to non-dissociative population transfer.

Acknowledgements

JK and RGB thank the Academy of Finland and the University of Helsinki for support of this work in the framework of the FiDiPro program. We thank also the Finnish CSC Center for the computational resources provided. RBG is also supported by the Israel Science Foundation (grant 172/12) and the National Science Foundation (CHE-090-9227). DF acknowledges the University of California, Irvine's Undergraduate Research Opportunities Program for support.

References

1 W.-L. Ting, Y.-H. Chen, W. Chao, M. C. Smith and J. J.-M. Lin, *Phys. Chem. Chem. Phys.*, 2014, **16**, 10438–10443.
2 R. Criegee, *Angew. Chem. Int. Ed. Engl.*, 1975, **14**, 745–752.
3 L. Vereecken, H. Harder and A. Novelli, *Phys. Chem. Chem. Phys.*, 2012, **14**, 14682.
4 Y. Sakamoto, S. Inomata and J. Hirokawa, *J. Phys. Chem. A*, 2013.
5 C. A. Taatjes, D. E. Shallcross and C. J. Percival, *Phys. Chem. Chem. Phys.*, 2014, **16**, 1704–1718.
6 C. A. Taatjes, G. Meloni, T. M. Selby, A. J. Trevitt, D. L. Osborn, C. J. Percival and D. E. Shallcross, *J. Am. Chem. Soc.*, 2008, **130**, 11883–11885.
7 O. Welz, J. D. Savee, D. L. Osborn, S. S. Vasu, C. J. Percival, D. E. Shallcross and C. A. Taatjes, *Science*, 2012, **335**, 204–207.
8 L. Sheps, *J. Phys. Chem. Lett.*, 2013, **4**, 4201–4205.
9 W.-L. Ting, C.-H. Chang, Y.-F. Lee, H. Matsui, Y.-P. Lee and J. J.-M. Lin, *J. Chem. Phys.*, 2014, **141**, 104308.
10 M. S. Alam, M. Camredon, A. R. Rickard, T. Carr, K. P. Wyche, K. E. Hornsby, P. S. Monks and W. J. Bloss, *Phys. Chem. Chem. Phys.*, 2011, **13**, 11002.
11 Y.-T. Su, Y.-H. Huang, H. A. Witek and Y.-P. Lee, *Science*, 2013, **340**, 174–176.
12 M. C. McCarthy, L. Cheng, K. N. Crabtree, O. Martinez, T. L. Nguyen, C. C. Womack and J. F. Stanton, *J. Phys. Chem. Lett.*, 2013, **4**, 4133–4139.
13 M. Nakajima and Y. Endo, *J. Chem. Phys.*, 2013, **139**, 101103.
14 C. C. Womack, M.-A. Martin-Drumel, G. G. Brown, R. W. Field and M. C. McCarthy, *Sci. Adv.*, 2015, **1**, e1400105–e1400105.
15 J. M. Beames, F. Liu, L. Lu and M. I. Lester, *J. Am. Chem. Soc.*, 2012, **134**, 20045–20048.
16 J. M. Beames, F. Liu, L. Lu and M. I. Lester, *J. Chem. Phys.*, 2013, **138**, 244307–244307–9.
17 M. C. Smith, W.-L. Ting, C.-H. Chang, K. Takahashi, K. A. Boering and J. J.-M. Lin, *J. Chem. Phys.*, 2014, **141**, 074302.
18 L. Sheps, A. M. Scully and K. Au, *Phys Chem Chem Phys*, 2014, **16**, 26701–26706.
19 C. A. Taatjes, O. Welz, A. J. Eskola, J. D. Savee, A. M. Scheer, D. E. Shallcross, B. Rotavera, E. P. F. Lee, J. M. Dyke, D. K. W. Mok, D. L. Osborn and C. J. Percival, *Science*, 2013, **340**, 177–180.

20 F. Liu, J. M. Beames, A. M. Green and M. I. Lester, *J. Phys. Chem. A*, 2014, **118**, 2298–2306.
21 H.-Y. Chen, C.-Y. Lien, W.-Y. Lin, Y. T. Lee and J. J. Lin, *Science*, 2009, **324**, 781–784.
22 R. Dawes, B. Jiang and H. Guo, *J. Am. Chem. Soc.*, 2015, **137**, 50–53.
23 E. Miliordos, K. Ruedenberg and S. S. Xantheas, *Angew. Chem. Int. Ed.*, 2013, **52**, 5736–5739.
24 Q. Meng and H.-D. Meyer, *J. Chem. Phys.*, 2014, **141**, 124309.
25 M. W. Schmidt, K. K. Baldridge, J. A. Boatz, S. T. Elbert, M. S. Gordon, J. H. Jensen, S. Koseki, N. Matsunaga, K. A. Nguyen, S. Su, T. L. Windus, M. Dupuis and J. A. Montgomery, *J. Comput. Chem.*, 1993, **14**, 1347–1363.
26 M. S. Gordon and M. W. Schmidt, in *Theory and Applications of Computational Chemistry, the First Forty Years*, eds. C. E. Dykstra, G. Frenking, K. S. Kim and G. E. Scuseria, Elsevier, Amsterdam, 2005, vol. Chapter 41, pp. 1167–1189.
27 J. Kalinowski, M. Räsänen and R. B. Gerber, *Chem. Phys. Lett.*, 2012, **535**, 44–48.
28 J. Kalinowski, M. Räsänen, P. Heinonen, I. Kilpeläinen and R. B. Gerber, *Angew. Chem. Int. Ed.*, 2014, **53**, 265–268.
29 D. Stone, M. Blitz, L. Daubney, T. Ingham and P. Seakins, *Phys. Chem. Chem. Phys.*, 2013, **15**, 19119.
30 A. Masaki, S. Tsunashima and N. Washida, *J. Phys. Chem.*, 1995, **99**, 13126–13131.
31 A. J. Eskola, D. Wojcik-Pastuszka, E. Ratajczak and R. S. Timonen, *Phys. Chem. Chem. Phys.*, 2006, **8**, 1416.
32 Z. J. Buras, R. M. I. Elsamra and W. H. Green, *J. Phys. Chem. Lett.*, 2014, **5**, 2224–2228.
33 R. Chhantyal-Pun, A. Davey, D. E. Shallcross, C. J. Percival and A. J. Orr-Ewing, *Phys. Chem. Chem. Phys.*, 2015, **17**, 3617–3626.
34 S. Enami, J. Ueda, M. Goto, Y. Nakano, S. Aloisio, S. Hashimoto and M. Kawasaki, *J. Phys. Chem. A*, 2004, **108**, 6347–6350.
35 S. Enami, Y. Sakamoto, T. Yamanaka, S. Hashimoto, M. Kawasaki, K. Tonokura and H. Tachikawa, *Bull. Chem. Soc. Jpn.*, 2008, **81**, 1250–1257.
36 T. J. Gravestock, M. A. Blitz, W. J. Bloss and D. E. Heard, *ChemPhysChem*, 2010, **11**, 3928–3941.
37 E. S. Foreman and C. Murray, *J. Phys. Chem. A*, 2015, **119**, 8981–8990.
38 J. Carlos Gómez Martín, P. Spietz and J. P. Burrows, *J. Photochem. Photobiol. Chem.*, 2005, **176**, 15–38.
39 P. Spietz, J. C. Gómez Martín and J. P. Burrows, *J. Photochem. Photobiol. Chem.*, 2005, **176**, 50–67.
40 E. P. F. Lee, D. K. W. Mok, D. E. Shallcross, C. J. Percival, D. L. Osborn, C. A. Taatjes and J. M. Dyke, *Chem. – Eur. J.*, 2012, **18**, 12411–12423.
41 *PGOPHER, a Program for Simulating Rotational Structure, C. M. Western, University of Bristol, http://pgopher.chm.bris.ac.uk*, PGOPHER, a Program for Simulating Rotational Structure, C. M. Western, University of Bristol, http://pgopher.chm.bris.ac.uk.
42 F. Liu, J. M. Beames, A. M. Green and M. I. Lester, *J. Phys. Chem. A*, 2014, **118**, 2298–2306.
43 J. H. Lehman, H. Li, J. M. Beames and M. I. Lester, *J. Chem. Phys.*, 2013, **139**, 141103.
44 K. Samanta, J. M. Beames, M. I. Lester and J. E. Subotnik, *J. Chem. Phys.*, 2014, **141**, 134303.
45 S. J. Strickler and R. A. Berg, *J. Chem. Phys.*, 1962, **37**, 814–822.

Figure Captions

Figure 1. Previous measurements of the CH_2OO $\tilde{B}^1A'$–$\tilde{X}^1A'$ transition. Beames *et al.* measured ionization depletion at discrete pump wavelengths, while Sheps and Ting *et al.* used cavity-enhanced and conventional absorption spectroscopy, respectively.

Figure 2. a) LED intensity profiles. b) Broadband absorption spectra collected with photolysis-probe time delays of 10 μs (black, offset vertically) and 100 μs (red, scaled by 0.55). c) CH_2OO absorption spectrum after subtraction of the IO contribution (black). An expanded view of the 376–406 nm region is shown in the inset. Grey shading represents 1σ uncertainty.

Figure 3. a) Cavity ring-down spectra recorded with photolysis-probe delays of 8 μs delay (black) and 140 μs (red, scaled by 0.15). b) CH_2OO absorption spectrum after subtraction of the IO contribution. Grey shading represents 1σ uncertainty.

Figure 4. Absolute absorption cross sections of the $\tilde{B}^1A'$–$\tilde{X}^1A'$ transition of CH_2OO from broadband transient absorption spectroscopy (black), and cavity ring-down spectroscopy (green). Previous measurements of the absorption cross sections by Beames et al. (orange), Sheps (red), and Ting et al. (blue) are shown for comparison. Grey shading represents 1σ uncertainty in the broadband measurement.

Figure 5. PGOPHER simulations of a single vibronic band of the $\tilde{B}^1A'$–$\tilde{X}^1A'$ transition of CH_2OO. The spectrum was simulated as *a*-type (blue) and *b*-type (red) transitions. The lineshape assumes a Gaussian component equivalent to the dye laser linewidth (0.08 cm^{-1}) and a Lorentzian component to model homogeneous broadening associated with excited state lifetimes of 10 ps, 1 ps and 0.1 ps, as indicated.

Figure 6. Temperature dependence of the CH_2OO absorption spectrum over the range 276–357 K. Spectra have been offset for clarity. Grey shading represents 1σ uncertainty.

Tables

Table 1. CH_2OO band centers and widths derived from the broadband transient absorption spectrum.

Band Center / cm^{-1} (Ting *et al.*)	Band Center / cm^{-1} (This Work)	FWHM / cm^{-1}
–	23196(13)	140(40)
23780	23849(9)	266(28)
24430	24469(7)	385(36)
25060	25131(6)	417(39)
25690	25716(8)	317(41)
26270	26313(7)	363(50)
26880	26885(11)	334(67)
27500	27452(25)	188(119)

Table 2. Harmonic vibrational frequencies calculated using MRCI and TD-DFT.[40]

		$\tilde{X}^1A'$		$\tilde{B}^1A'$		
	Mode	MRCI	TD-DFT	MRCI	TD-DFT	Assignment
a′	ν_1	3360	3220	3255	3291	a-CH str.
	ν_2	3220	3116	4043	3128	s-CH str.
	ν_3	1515	1537	1520	1692	CH_2 sc./CO str.
	ν_4	1255	1404	2664	1459	CO str./CH_2 sc.
	ν_5	1203	1240	1230	1154	CH_2 rock
	ν_6	1005	898	953	893	OO str.
	ν_7	561	528	462	441	COO bend
a″	ν_8	742	943	1662	1334	CH_2 wag
	ν_9	642	669	1440	651	CH_2 twist

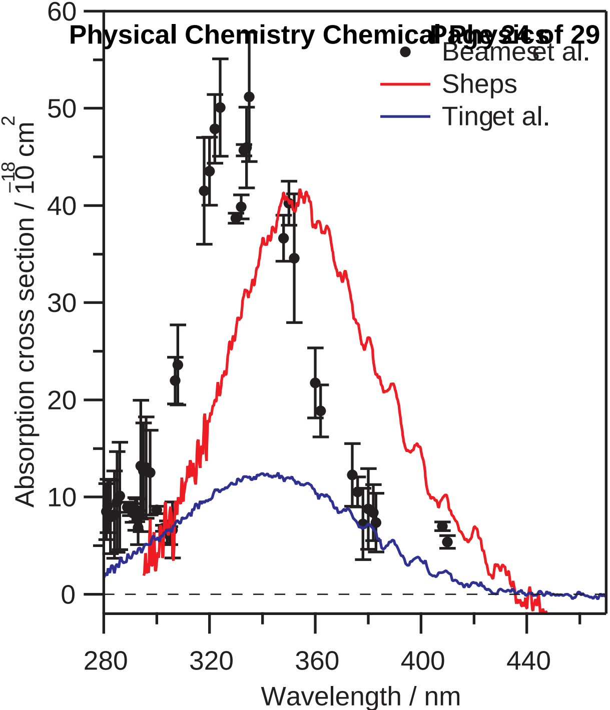
Beames et al.
Sheps
Ting et al.
Absorption cross section / 10^{-18} cm^2
0
10
20
30
40
50
60
280
320
360
400
440
Wavelength / nm

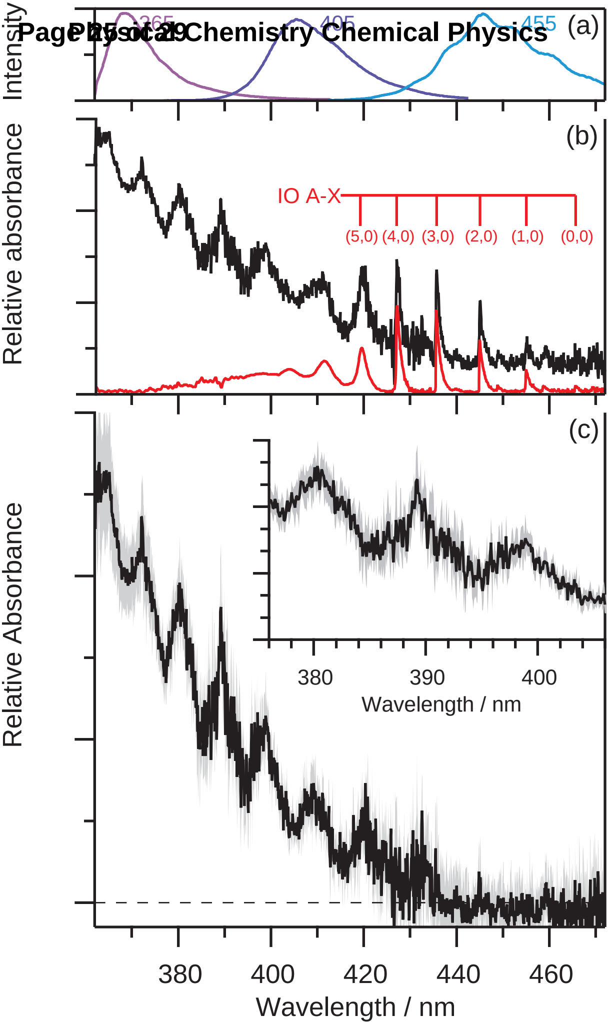
Intensity
365
405
455
(a)
Relative absorbance
(b)
IO A-X
(5,0)
(4,0)
(3,0)
(2,0)
(1,0)
(0,0)
Relative Absorbance
(c)
380
390
400
Wavelength / nm
380
400
420
440
460
Wavelength / nm

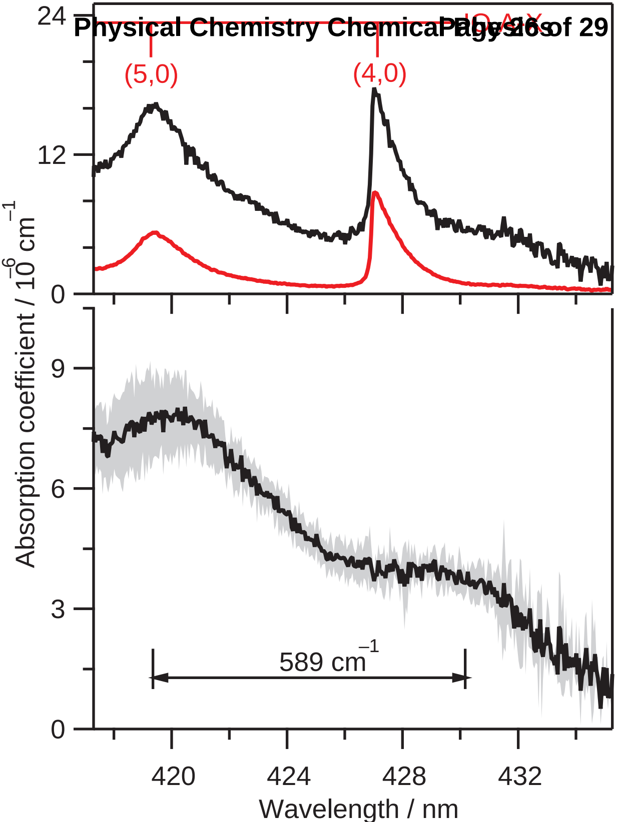
IO A-X
(5,0)
(4,0)
24
12
0
9
6
3
0
Absorption coefficient / 10^{-6} cm^{-1}
589 cm^{-1}
420
424
428
432
Wavelength / nm

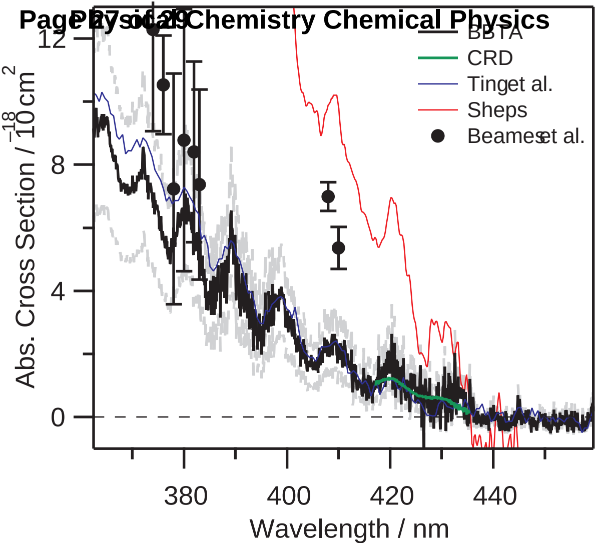
BBTA
CRD
Ting et al.
Sheps
Beames et al.
Abs. Cross Section / 10^{-18} cm^2
12
8
4
0
380
400
420
440
Wavelength / nm

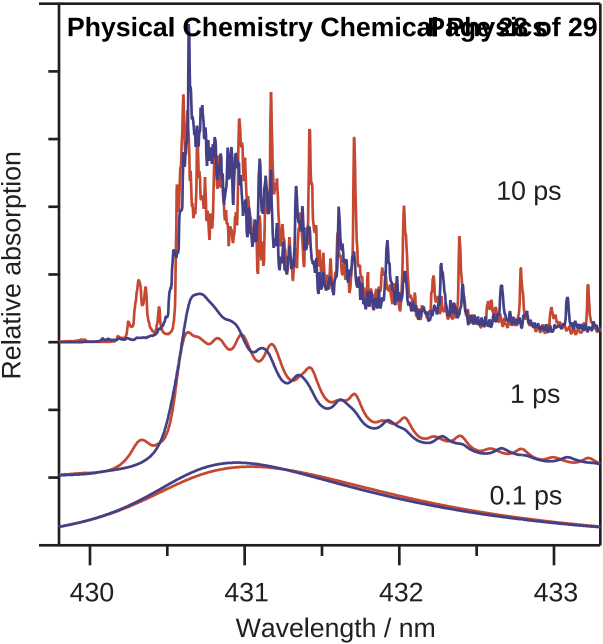
Relative absorption
10 ps
1 ps
0.1 ps
430
431
432
433
Wavelength / nm

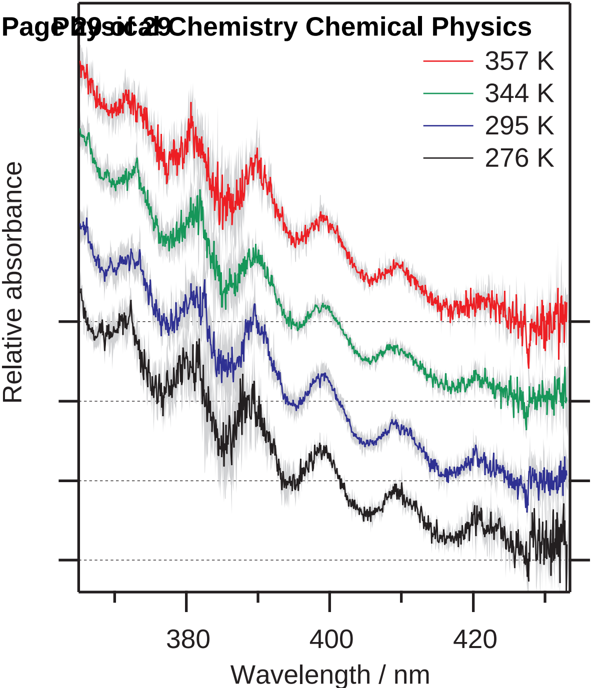
357 K
344 K
295 K
276 K
Relative absorbance
380
400
420
Wavelength / nm